RSC Advances

ROYAL SOCIETY OF CHEMISTRY

www.rsc.org/advances

Graphical Abstract

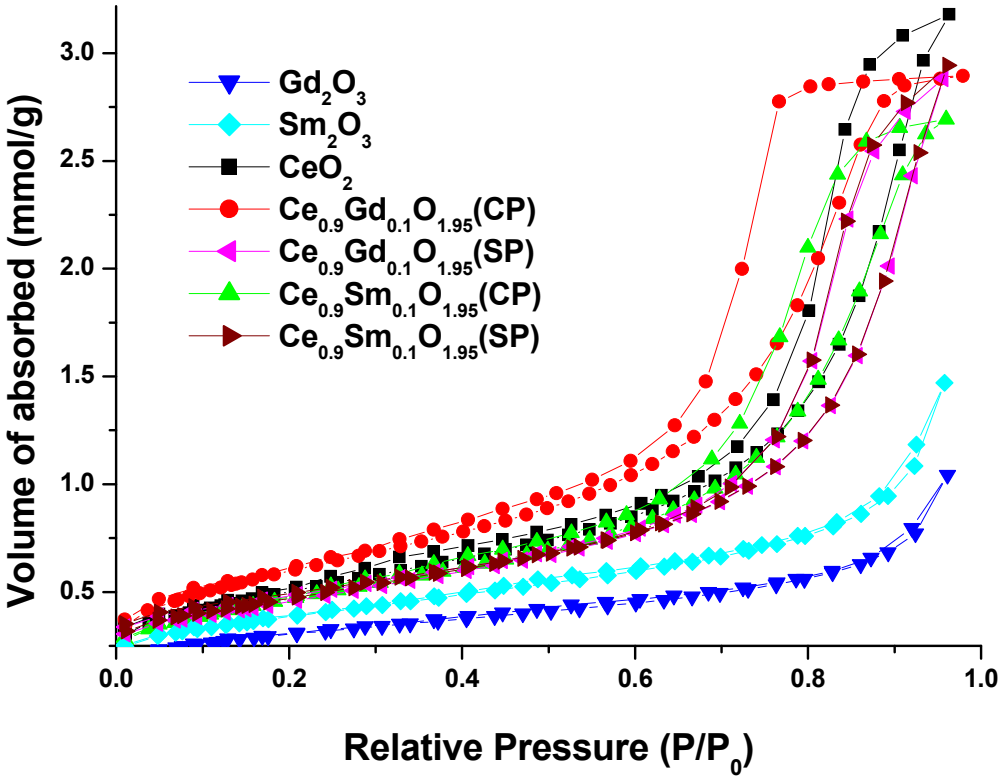

Low frequency ultrasound assisted sequential and co-precipitation of nanoporous RE (Gd and Sm) doped Cerium oxide

Panneerselvam Sathishkumar[a,b]*, Ramalinga Viswanathan Mangalaraja[a]*, Thangaraj Pandiyarajan[a], M. A. Gracia-Pinilla[c,d] N. Escalona[e], C. Herrera[e], R. Garcia[e]

[a]Advanced Ceramics and Nanotechnology Laboratory, Department of Materials Engineering, Faculty of Engineering, University of Concepcion, Concepcion 407-0409, Chile

[b]Department of Chemistry, Periyar Maniammai University, Vallam, Thanjavur – 613403, Tamil Nadu, India

[c]Universidad Autónoma de Nuevo León, Facultad de Ciencias Físico-Matemáticas, Av. Universidad, Cd. Universitaria, San Nicolás de los Garza, N.L. México.

[d]Universidad Autónoma de Nuevo León, Centro de Investigación e Innovación en Desarrollo de Ingeniería y Tecnología, Avenida Alianza 101 Sur PIIT Monterrey Apodaca, NL66600, Mexico

[e]Faculty of Chemical Sciences, University of Concepcion, PO Box 160-C, Correo 3, Concepcion, Chile

*Corresponding Authors Address:
Advanced Ceramics and Nanotechnology Laboratory, Department of Materials Engineering, Faculty of Engineering, University of Concepcion, Concepcion 407-0409, Chile. Tel.: +56 41 2207389; fax: +56 41 2203391.
E-mail addresses:
sathish_panner2001@yahoo.com (P. Sathishkumar), mangal@udec.cl (R.V. Mangalaraja).

ABSTRACT

The 42 kHz ultrasound assisted cerium oxide (CeO_2), $Ce_{0.9}Gd_{0.1}O_{1.95}$ and $Ce_{0.9}Sm_{0.1}O_{1.95}$ nanostructure were synthesized using sequential and co-precipitation techniques. The nanoporous nature of the powders was revealed from the BET analysis that the observed pore size distribution and the H2 hysteresis loop of the respective nanostructures confirmed the existence of nanopores in various size and shape. The nanoporous nature of the synthesized powders were further confirmed by the high resolution transmission electron microscopy (HRTEM) and high angle annular dark field (HAADF) scanning transmission electron microscopy (STEM) analyses. The perceived shift in the characteristic F_{2g} Raman active band centered at 464 cm^{-1} indicated the defects were increased during the sequential and co-precipitation of $Ce_{0.9}Gd_{0.1}O_{1.95}$ and $Ce_{0.9}Sm_{0.1}O_{1.95}$ nanostructures. Moreover, the intensity of the F_{2g} peaks can be ordered as CeO_2 < $Ce_{0.9}Sm_{0.1}O_{1.95}$ (CP)[1] < $Ce_{0.9}Gd_{0.1}O_{1.95}$ (SP)[2] < $Ce_{0.9}Sm_{0.1}O_{1.95}$ (SP)[2] < $Ce_{0.9}Gd_{0.1}O_{1.95}$ (CP)[1] that indicated the increase in the concentration of the defects like oxygen vacancies to enhance the efficiency of the solid oxide fuel cells (SOFCs) as electrolyte materials. The diffuse reflectance UV-vis solid state spectroscopic analysis demonstrated the narrowing the optical band gap of CeO_2 during the sequential and co-precipitation of the $Ce_{0.9}Gd_{0.1}O_{1.95}$ and $Ce_{0.9}Sm_{0.1}O_{1.95}$ nanostructures.

Key words: 42 kHz ultrasound, rare earth doped ceria, nanoporous

[1]Co-precipitation
[2]Sequential precipitation

1. Introduction

The incessant usage of the non-renewable energy resources leads to initiate two major threats to the economy of the developing countries namely, scarcity and the cost of the fossil fuels. The second and most important issue is the environmental pollution associated with the usage of the fossil fuels which leads to unpredictable perilous effects throughout the world. To avoid the deleterious effects, fuel cell (FC) is an electrochemical device which affords the non-polluting, higher energy density and efficient when compared to any other energy storage devices being practiced [1-2]. Among the various categories of FCs, solid oxide fuel cells (SOFCs) become easier for the portable and stationary practices however the operating temperature needs to be reduced to improve the frequent implements of the next generation SOFCs. The operating principle of the SOFC can be simply explained as follows: the conversion of fuel into ions and electrons at the anode followed by the reaction of ions with the oxidants at the cathode [2,3]. The electrolyte packed between the anode and cathode generates the transport of the oxygen ions, which endorses the efficiency of the SOFCs [4]. The enhanced physicochemical characteristics of the electrolytes certainly increase the efficiency of the SOFCs. The large scale preparation of the electrolytes through economically viable methodologies makes the electrolyte materials in-expensive.

The nanomaterials synthesized by the ultrasound assisted technique exhibited various interesting and unconventional physicochemical characteristics. The utilization of low frequency or power ultrasound (20 – 100 kHz) has been significantly increased in the recent years for various applications [5-9]. The extreme conditions (high temperature and pressure) produced during the irradiation of ultrasound generate the non-selective free

radicals within the aqueous medium which accelerates the chemical reaction among the precursors and enhances the physicochemical characteristics of the subsequent nanomaterials. On the other hand, cerium dioxide (CeO_2) is a highly refractive ceramic material which is utilized for the various applications of day-today life [10-15]. The CeO_2 and modified CeO_2 electrolytes possessing the interesting features for SOFC. The balanced behaviour of Ce^{3+}/Ce^{4+} generates the significant contribution of CeO_2 in SOFC applications. The doping of rare earth ions into the CeO_2 significantly increases the oxygen vacancies and oxygen storage properties of the resulting electrolytes [16,17]. Nevertheless, the loading of RE_2O_3 into CeO_2 enhances the oxygen ion conductivity and the mechanical properties of the resultant nanomaterials [18,19].

CeO_2 and the modified CeO_2 nanomaterials prepared by using various procedures such as precipitation [20], hydrothermal [21], spray-pyrolysis [22], sol-gel [23] and combustion [24] were reported in the literature. The low frequency ultrasound assisted synthesis of CeO_2 and the modified CeO_2 nanomaterials was expected to modify the physicochemical characteristics and to improve the thermal and mechanical properties of the resulting solid electrolytes. In the present work, CeO_2, $Ce_{0.9}Gd_{0.1}O_{1.95}$ and $Ce_{0.9}Sm_{0.1}O_{1.95}$ nanostructures were synthesized by using 42 kHz ultrasound. The effect of sequential and co-precipitation on the structural, morphological and optical properties of the $Ce_{0.9}Gd_{0.1}O_{1.95}$ and $Ce_{0.9}Sm_{0.1}O_{1.95}$ nanostructures was investigated. The developed methodology can be extended for the preparation of the various nanomaterials.

2. Experimental

2.1. Materials and methods

Nitrates of cerium, gadolinium and samarium, and sodium hydroxide were purchased from the Sigma-Aldrich and used as starting materials for the synthesis of CeO_2, $Ce_{0.9}Gd_{0.1}O_{1.95}$ and $Ce_{0.9}Sm_{0.1}O_{1.95}$ nanostructures without further purification. Unless otherwise specified, all reagents used were of analytical grade and the solutions were prepared using double distilled water. The crystallite size of the synthesized nanomaterials was calculated from the X-ray diffraction data (XRD, Philips PW1710 diffractometer, CuK_α radiation, Holland) using Scherrer equation. Surface morphology and microstructure of the nanostructures were analyzed by transmission electron microscopy (HRTEM, FEI TITAN G2 80-300) operated at 300 keV. Diffuse reflectance UV-Vis spectra of the nanostructures were recorded using a Shimadzu 2550 spectrophotometer equipped with an integrating sphere accessory employing $BaSO_4$ as reference material. Raman spectra were recorded using a Dilor LabRam-1B spectrometer, with 633 nm line of He-Ne laser source with 5.5 mW powers. The surface area, pore volume and pore diameter of the nanostructutres were measured with the assistance of Flowsorb II 2300 of Micrometrics, Inc. The sonochemical reactions in this study were carried out by using a commercially available sonicator (8890, Cole-Parmer, USA) producing 42 kHz ultrasonic waves.

2.2. Preparation of CeO_2, $Ce_{0.9}Gd_{0.1}O_{1.95}$ and $Ce_{0.9}Sm_{0.1}O_{1.95}$ nanostructures

The co-precipitation of $Ce_{0.9}Gd_{0.1}O_{1.95}$ was carried out according to the procedure that we have reported earlier [25]. For sequential precipitation, a slight modification in the synthesis procedure was carried out as follows: the appropriate quantity of the nitrate precursor of gadolinium and CeO_2 was added to the 200 mL of double distilled water under vigorous stirring for 15 min. 50 mL of 1M NaOH was prepared separately. The sonicator was turned on and the time was taken as “time zero” for ultrasound irradiation along with

the drop-wise addition of NaOH to the nitrate precursor under vigorous stirring. The ultrasound irradiation of the suspension was continued for 30 min. The solid solution was collected by the subsequent filtration (0.45 μm nylon membrane filters). The solid solution was dried at 110ºC for 12 h followed by the calcination at 700ºC for 2 h. Similar procedure was adopted for the preparation of $Ce_{0.9}Sm_{0.1}O_{1.95}$,CeO_2, Gd_2O_3 and Sm_2O_3 nanostructures. The stoichiometric concentration of CeO_2 and nitrate precursors of gadolinium and samarium was taken for the sequential precipitation of $Ce_{0.9}Gd_{0.1}O_{1.95}$ and $Ce_{0.9}Sm_{0.1}O_{1.95}$ nanocomposites.

3. Results and discussion

The X-ray diffraction analysis of the nanomaterials synthesized using low frequency ultrasound is presented in Fig.1. The formation of cubic structured Gd_2O_3 and Sm_2O_3 were identified according to the JCPDS numbers 74-1807 and 11-0608, respectively. The bare Sm_2O_3 demonstrated the poor crystalline nature when compared to the bare Gd_2O_3. The bare CeO_2 exhibited cubic fluorite crystal structure (JCPDS no. 34-0394) as evidenced from Fig.1. The sequential and co-precipitation of $Ce_{0.9}Gd_{0.1}O_{1.95}$, $Ce_{0.9}Sm_{0.1}O_{1.95}$ revealed that the cubic fluorite crystal structure of CeO_2 was not altered during the synthesis of the nanomaterials. The CeO_2 diffraction pattern was dominated in the doped nanomaterials resulted from the sequential and co-precipitated cerium (Ce^{4+}) and dopant rare earth (Gd^{3+} and Sm^{3+}) precursors. The observed strategy confirmed that the Gd^{3+} and Sm^{3+} entered into the crystal lattice of CeO_2 which can be evidenced from the absence of corresponding diffraction pattern of dopant rare earth oxides. However, the penetration of Gd^{3+} and Sm^{3+} in the sequentially precipitated nanostructures was likely entered during the calcination and there was no core shell structure observed. Besides, further analysis is needed to confirm

the morphology and crystal structure of the sequential and co-precipitated $Ce_{0.9}Gd_{0.1}O_{1.95}$ and $Ce_{0.9}Sm_{0.1}O_{1.95}$ nanostructures.

The Raman spectra observed for the (co-precipitation and sequential precipitation) prepared nanostructures are shown in Fig. 2 which suggested the vibrational changes occurred due to the introduction of rare earth oxides into the crystal structure of CeO_2. The cubic fluorite crystal structure for the CeO_2, $Ce_{0.9}Gd_{0.1}O_{1.95}$ and $Ce_{0.9}Sm_{0.1}O_{1.95}$ can be identified from the strong and intensive Raman active (F_{2g}) bands at 455–470 cm^{-1}. The oxygen vacancies in the crystal structure of CeO_2 can be understood from the two less intensive bands appeared at the range of 250–290 and 605–625 cm^{-1} [26]. The CeO_2 showed its characteristic F_{2g} Raman active band centered at 464 cm^{-1}, the sequentially and co-precipitated $Ce_{0.9}Gd_{0.1}O_{1.95}$ and $Ce_{0.9}Sm_{0.1}O_{1.95}$ nanostructures showed ~ ± 2 nm shift in the F_{2g} Raman active band for the cubic fluorite structure (insert of Fig. 2). The observed decrease in the intensity of F_{2g} band showed the increase in the concentration of the defects like oxygen vacancies [29]. The intensive Raman bands observed at 361 (B_g) and 345 cm^{-1} (A_g and F_g modes) suggested the cubic crystal structure for the $Gd_2O_3$and Sm_2O_3 [27,28]. The absence of the Raman active modes of Gd_2O_3 (361 cm^{-1}), Sm_2O_3 (345 cm^{-1}) and the shift observed at the F_{2g} Raman active band for the cubic fluorite crystal structure (464 cm^{-1}) clearly designated the entry of the rare earths into the crystal structure of CeO_2. On the other hand, the intensity of the F_{2g} peaks can be ordered as follows: CeO_2 < $Ce_{0.9}Sm_{0.1}O_{1.95}$ (CP)[3] < $Ce_{0.9}Gd_{0.1}O_{1.95}$ (SP)[4] < $Ce_{0.9}Sm_{0.1}O_{1.95}$ (SP)[2] < $Ce_{0.9}Gd_{0.1}O_{1.95}$ (CP)[1].

[3]Co-precipitation
[4]Sequential precipitation

The representative HRTEM micrographs observed for the bare CeO_2, Gd_2O_3 and Sm_2O_3 are presented in Fig. 3. The CeO_2 exhibited the nanoparticle morphology and the average grain size was ~ 20 nm (Fig. 3a). The finger print lattice fringe distance was calculated as 0.31 nm (Fig. 3b) which corresponds to the (1 1 1) crystal plane of cubic fluorite structure of CeO_2. The Gd_2O_3 and Sm_2O_3 revealed the nanorod morphology of several nanometers in length and thickness along with approximately 15% of nanoparticle (Figs. 3c and 3e). The finger print lattice fringe distance were calculated as 0.31 nm and 0.32 for the corresponding (2 2 2) crystal planes of Gd_2O_3 (Fig. 3d) and Sm_2O_3 (Fig. 3f), respectively. The HRTEM micrographs of the sequential and co-precipitated $Ce_{0.9}Gd_{0.1}O_{1.95}$ and $Ce_{0.9}Sm_{0.1}O_{1.95}$ nanostructures demonstrated the formation of clear internal crystal lattice structures (Figs. 4 and 5). Thus confirmed the high crystallinity was achieved during the synthesis of the nanomaterials. The HRTEM micrographs (Fig. 4) of the sequential (a-c) and co-precipitated (d-f) $Ce_{0.9}Gd_{0.1}O_{1.95}$ nanostructures demonstrated the significant magnitude of bare Gd_2O_3 nanorods (Fig 3c) was transformed to the nanoparticle morphology.

The HRTEM micrographs (Fig. 5) of the sequentially precipitated (a-c) $Ce_{0.9}Sm_{0.1}O_{1.95}$ nanostructures showed the 25% nanorod morphology whereas the co-precipitated (d-f) $Ce_{0.9}Sm_{0.1}O_{1.95}$ nanostructures showed only 5% of nanorod morphology. However, the ratio of the nanorod versus nanoparticle was significantly decreased when compared to the bare Sm_2O_3 (Fig. 3e). Similar kind of surface distribution of samarium was detected on the surface of CeO_2 when compared with the $Ce_{0.9}Gd_{0.1}O_{1.95}$. Thus confirmed that the 42 kHz low frequency ultrasound was adequate to provoke the initiation of $Ce_{0.9}Gd_{0.1}O_{1.95}$ and $Ce_{0.9}Sm_{0.1}O_{1.95}$ nanostructures from the precursors. The grain size

achieved for the $Ce_{0.9}Gd_{0.1}O_{1.95}$ (Figs. 4a and 4d) and $Ce_{0.9}Sm_{0.1}O_{1.95}$ (Figs. 5a and 5d) nanopowders was calculated ~ 10 nm from the HRTEM analysis. The calculated grain size from the HRTEM was in good agreement with the grain size calculated from the XRD using Debye-Scherrer equation. The observed decrease in the grain size suggested the increase in the defects of individual nanomaterials [30].

The formation of nanoporous structures is shown in Figs. 4b, 4c, 4f, 5c, 5e and 5f (circled). The HRTEM micrographs additionally demonstrated the formation of $Ce_{0.9}Gd_{0.1}O_{1.95}$ and $Ce_{0.9}Sm_{0.1}O_{1.95}$ when the precursor underwent the ultrasonic irradiation. The sequentially precipitated exhibited the greater number of nanopores when compared to the co-precipitated materials. The formation of nanoporous structure was not observed for the bare Gd_2O_3 and Sm_2O_3 under the same laboratory conditions. The nanopore structured CeO_2 was noticed from Fig. 3a, however the HRTEM analysis evidently suggested the number of nanopores of CeO_2 was found to increase during the synthesis of the rare earth doped CeO_2.

The high angle annular dark field scanning transmission electron microscopy (HAADF-STEM) analysis of the sonochemically synthesized $Ce_{0.9}Gd_{0.1}O_{1.95}$ and $Ce_{0.9}Sm_{0.1}O_{1.95}$ revealed the formation of nanopore structures which can be easily identified as the black blotches in the micrographs (Figs. 6a and 6b & Figs. 7a and 7b). The diameter of the nanopores was measured as ~ 1 to 2 nm during the HAADF-STEM analysis. The sequentially precipitated $Ce_{0.9}Gd_{0.1}O_{1.95}$ and $Ce_{0.9}Sm_{0.1}O_{1.95}$ exhibited large number of nanopores when compared to the co-precipitated nanostructures. The HAADF emission confirmed the formation $Ce_{0.9}Gd_{0.1}O_{1.95}$ and $Ce_{0.9}Sm_{0.1}O_{1.95}$ and no other phases belong to the impurities were detected. The EDX analysis of the corresponding nanomaterialsis

presented in Figs. 6c and 6d &Fig. 7c and 7d. The elemental analysis designated the stoichiometric ratio of the nanomaterials.

The Brunar Emmett and Teller (BET) analysis was performed for the sonochemically synthesized nanostructures to understand the various structural and textural properties of CeO_2, sequential and co-precipitated $Ce_{0.9}Gd_{0.1}O_{1.95}$ and $Ce_{0.9}Sm_{0.1}O_{1.95}$. Fig. 8 shows the type IV adsorption-desorption profile achieved for all the sonochemically synthesized nanopowders. The CeO_2, $Ce_{0.9}Gd_{0.1}O_{1.95}$ and $Ce_{0.9}Sm_{0.1}O_{1.95}$ adsorption-desorption profiles demonstrated the narrow H_2 type hysteresis loop and it was not observed for Gd_2O_3 and Sm_2O_3. The observed H_2 type hysteresis loop revealed the complex pore structure which can also be evidenced from the HRTEM and HAADF-STEM analyses. The surface area and the various parameters associated with the pores are presented in Table 1which illustrates the decrease in the surface area for the sequentially precipitated $Ce_{0.9}Gd_{0.1}O_{1.95}$ and $Ce_{0.9}Sm_{0.1}O_{1.95}$ when compared to the bare CeO_2. Besides, the Barrett-Joyner-Halenda (BJH) analysis (Fig. 9) showed that the pore volume distribution attained for the bare CeO_2 was not significantly altered during the sequential precipitation. However, the H_2 hysteresis observed for co-precipitated rare earth doped ceria was broadened (Fig.8) than the bare CeO_2. The surface area and pore diameter for the co-precipitated $Ce_{0.9}Gd_{0.1}O_{1.95}$ and $Ce_{0.9}Sm_{0.1}O_{1.95}$ were modified when compared to the bare CeO_2 (Table 1 and Fig. 9). The considerable changes occurred during co-precipitation designated the different sized and shaped nanopores were formed [31] under the low frequency ultrasound assisted process. Moreover, Table 1 clarifies the various nanopore properties of the synthesized nanostructures.

The diffuse reflectance (DR) UV-vis spectral analysis of the synthesized nanostructures is presented in Fig. 10. The bare Gd_2O_3 and Sm_2O_3 showed its absorption maximum in the ultraviolet region and the absorption of bare CeO_2 can be indexed in the visible light region. The characteristic visible light absorption of the bare CeO_2 considerably demonstrated the defects (Fluorite crystal structure) got increased during the ultrasound irradiations which lead to shift the characteristic absorption when compared to the commercial CeO_2 [32]. The absence of the characteristic absorption of Gd_2O_3 and Sm_2O_3 in the DR-UV-vis spectra additionally supported the formation of $Ce_{0.9}Gd_{0.1}O_{1.95}$ and $Ce_{0.9}Sm_{0.1}O_{1.95}$ in addition to the Raman and HRTEM analyses. The absorption band edge was blue shifted for the sequentially precipitated $Ce_{0.9}Gd_{0.1}O_{1.95}$ and $Ce_{0.9}Sm_{0.1}O_{1.95}$ whereas it was red shifted for the co-precipitated $Ce_{0.9}Gd_{0.1}O_{1.95}$ and $Ce_{0.9}Sm_{0.1}O_{1.95}$ when compared to the same observed for the bare CeO_2 (Fig. 10). The Tauc plot derived from Kubelka Munk function is shown in Fig. 11. The optical band gap for the bare CeO_2 was 2.228 eV which was significantly lower than the same reported for the commercial CeO_2 [32]. The optical band gap for the sequentially precipitated $Ce_{0.9}Gd_{0.1}O_{1.95}$ (2.321 eV) and $Ce_{0.9}Sm_{0.1}O_{1.95}$ (2.410 eV) was higher than the bare CeO_2 (2.228 eV). Besides, the co-precipitated $Ce_{0.9}Gd_{0.1}O_{1.95}$ (2.214 eV) and $Ce_{0.9}Sm_{0.1}O_{1.95}$ (2.212 eV) were showed the narrowing optical band gap than CeO_2. The respective modifications resulted in the $Ce_{0.9}Gd_{0.1}O_{1.95}$ and $Ce_{0.9}Sm_{0.1}O_{1.95}$ when compared to the optical band gap of bare Gd_2O_3 (5.05 eV), Sm_2O_3 (4.5 eV) and CeO_2 indicated the rare earth oxides acted as the band gap modifier during the ultrasound assisted sequential and co-precipitation.

4. Conclusion

The 42 kHz ultrasound assisted CeO_2, Gd_2O_3, Sm_2O_3, $Ce_{0.9}Gd_{0.1}O_{1.95}$ and $Ce_{0.9}Sm_{0.1}O_{1.95}$ nansostructures were successfully synthesized using sequential and co-precipitation techniques. The nanorod morphology of the Gd_2O_3 and Sm_2O_3 was transformed to the nanoparticle morphology during the preparation of $Ce_{0.9}Gd_{0.1}O_{1.95}$ and $Ce_{0.9}Sm_{0.1}O_{1.95}$. The HRTEM analysis significantly indicated the decrease in the grain size for the sequential and co-precipitated $Ce_{0.9}Gd_{0.1}O_{1.95}$ and $Ce_{0.9}Sm_{0.1}O_{1.95}$ than the bare CeO_2, Gd_2O_3 and Sm_2O_3. In accordance with the grain size, BET and BJH analyses illustrated the surface area, nanoporous texture and pore diameter of the rare earth doped nanoceria was rehabilitated when compared to the bare and commercially available CeO_2. Moreover, the observed shift in the Raman analysis and the band gap narrowing during the diffuse reflectance UV-vis investigation patronaged the defects (oxygen vacancies) increased in the $Ce_{0.9}Gd_{0.1}O_{1.95}$ and $Ce_{0.9}Sm_{0.1}O_{1.95}$ than the bare CeO_2, Gd_2O_3 and Sm_2O_3. The enhanced number of nanopores was identified from the HAADF-STEM analysis and the BET analysis demonstrated the pore diameter of the sequentially precipitated rare earth doped nanoceria was not significantly modified as influenced in the bare CeO_2 and co-precipitated rare earth doped nanoceria. Therefore, the ultrasound assisted synthesis of $Ce_{0.9}Gd_{0.1}O_{1.95}$ and $Ce_{0.9}Sm_{0.1}O_{1.95}$ will make significant contribution to improve the ion conducting properties which enhances the efficiency of the solid oxide fuel cells.

Acknowledgements

The authors would like to thank FONDECYT No.: 1130916 Government of Chile, Santiago, for financial assistance.

References

[1] N. Sammes N, editor. Fuel cell technology: reaching towards commercialization. London: Springer; 2006.

[2] A. Hermanna, T. Chaudhuria, P. Spagnol, Bipolar plates for PEM fuel cells: A review. Int. J. Hydrogen Energy 30 (2005) 1297-1302.

[3] S. Srinivasan, Fuel cells: from Fundamentals to applications. New York: Springer; 2006.

[4] S. P. Jiang, Development of lanthanum strontium manganite perovskite cathode materials of solid oxide fuel cells: a review. J. Mater. Sci. 43 (2008) 6799-6833.

[5] S. Pilli, P.Bhunia, S. Yan, R.J. LeBlanc, R.D. Tyagi, R.Y. Surampalli, Ultrasonic pretreatment of sludge: A review, Ultrason. Sonochem.18 (2011) 1-18.

[6] H.Okkay, M.Bayramoglu, M. F.Oksuzomer, $Ce_{0.8}Sm_{0.2}O_{1.9}$ synthesis for solid oxide fuel cell electrolyte by ultrasound assisted co-precipitation method, Ultrason. Sonochem.20 (2013) 978-983.

[7] S. Cho, J. Kim, J. Chun, J. Kim, Ultrasonic formation of nanobubbles and their zeta-potentials in aqueous electrolyte and surfactant solutions, Colloid. Surf. A physicochemical. Eng. 269 (2005) 28-34.

[8] Y. Wang, D. Zhao, W. Ma, C. Chen, J. Zhao, Enhanced sonocatalytic degradation of azo dyes by Au/TiO_2, Environ. Sci. Technol. 42 (2008) 6173-6178.

[9] P. Sathishkumar, R. V. Mangalaraja, H. D. Mansilla, M.A. Gracia-Pinilla, S. Anandan, Sonophotocatalytic (42 kHz) degradation of Simazine in the presence of Au-TiO_2 nanocatalysts, Appl. Catal. B: Environ. 160-161 (2014) 692-700.

[10] P. Trogadas, J. Parrondo, V. Ramani, Platinum supported on CeO_2 effectively scavenges free radicals within the electrolyte of an operating fuel cell, Chem. Commun. 47 (2011) 11549-11551.

[11] P. Jasinski, T. Suzuki, H.U. Anderson, Nanocrystallineundoped ceria oxygen sensor, Sensors and Actuators, B: Chemical 95 (2003) 73-77.

[12] T. Mori, J. Drennan, Influence of microstructure on oxide ionic conductivity in doped CeO_2 electrolytes, J. Electroceram. 17 (2012) 749-757.

[13] X. Lu, T. Zhai, H. Cui, H. Shi, S. Xie, Y. Huang, C. Liang, Y. Tong, Redox cycles promoting photocatalytic hydrogen evolution of CeO_2nanorods, J. Mater. Chem. 21 (2011) 5569-5572.

[14] S. Yabea, T. Satob, Cerium oxide for sunscreen cosmetics, J. Solid State Chem. 171 (2003) 7-11.

[15] J. F. de Lima, R.F. Martins, C.R. Neri, O.A. Serra, ZnO:CeO_2-based nanopowders with low catalytic activity as UV absorbers, Appl. Surf. Sci. 255 (2009) 9006-9009.

[16] B. Matović1, J. Dukić,A.Devečerski, S. Bošković,M.Ninić,Z.Dohčević-Mitrović, Crystal structure analysis of Nd-doped ceria solid solutions, Sci. Sinter. 40 (2008) 63-68.

[17] B. Choudhury, A. Choudhury, Lattice distortion and corresponding changes in optical properties of CeO_2 nanoparticles on Nd doping, Curr. Appl. Phys. 13 (2013) 217-223.

[18] T.S. Zhang, J. Ma, L.B. Kong, P. Hing, J.A. Kilner, Preparation and mechanical properties of dense $Ce_{0.8}Gd_{0.2}O_{2-\delta,}$ ceramics, Solid State Ionics 167 (2004) 191-196.

[19] A. Akbari-Fakhrabadi, R.V. Mangalaraja, F. A. Sanhueza, R. E. Avila, S. Ananthakumar, S. H. Chan, Nanostructured Gd-CeO_2 electrolyte for solid oxide fuel cell by aqueous tape casting, J. Power Sources 218 (2012) 307-312.

[20] A. I. Y. Tok, L. H. Luo, F. Y. C. Boey, Carbonate co-precipitation of Gd_2O_3-doped CeO_2 solid solution nano-particles, Mater. Sci. Eng. A 383 (2004) 229-234.

[21] F. Zhang, S. P. Yang, H. M. Chen, X. B. Yu, Preparation of discrete nano size ceria powder, Ceram. Int. 30 (2004) 997-1002.

[22] C. Goulart, E. Djurado, Synthesis and sintering of Gd-doped CeO_2nanopowders prepared by ultrasonic spray pyrolysis, J. Eur. Ceram. Soc. 33 (2013) 769-778.

[23] G. S. Wua, T. Xiea, X. Y. Yuana, B. C. Cheng, L. D. Zhang, An improved sol-gel template synthetic route to large-scale CeO_2 nanowires, Mater. Res. Bull. 39 (2004) 1023-1028.

[24] L. D. Jadhava, M. G. Chourashiya, K. M. Subhedar, A. K. Tyagi, J. Y. Patil, Synthesis of nanocrystalline Gd doped ceria by combustion technique, J. Alloys Compd. 470 (2009) 383-386.

[25] P. Sathishkumar, R. V. Mangalaraja, O. Rozas, H. D. Mansilla, M. A. Gracia-Pinilla, S. Anandan, Low frequency ultrasound (42 kHz) assisted degradation of Acid Blue 113 in the presence of visible light driven rare earth nanoclusters loaded TiO_2 nanophotocatalysts, Ultrason. Sonochem. 21 (2014) 1675-1681.

[26] R. Kydd, W. Y. Teoh, K. Wong, Y. Wang, J. Scott, Q. H. Zeng, A. B. Yu, J. Zou, R. Amal, Flame-synthesized ceria-supported copper dimers for preferential oxidation of CO, Adv. Funct. Mater. 2009, 19, 369-377.

[27] C. Le Luyer, A. Garcia-Murillo, E. Bernstein, J. Mugnier, Waveguide Raman spectroscopy of sol-gel Gd_2O_3 thin films, J. Raman Spec. 34 (2003) 234-239.

[28] S. Jiang, J. Liu, C. Lin, X. Li, Y. Li, High-pressure x-ray diffraction and Raman spectroscopy of phase transitions in Sm_2O_3, J. Appl. Phys. 113 (2013) 113502-06.

[29] X. Yao, C. Tang, Z. Ji, Y. Dai, Y. Cao, F. Gao, L. Dong, Y. Chen, Investigation of the physicochemical properties and catalytic activities of $Ce_{0.67}M_{0.33}O_2$(M = Zr^{4+}, Ti^{4+}, Sn^{4+}) solid solutions for NO removal by CO, Catal. Sci. Technol., 3(2013), 688-698.

[30] L. Ilieva, G. Pantaleo, I. Ivanov, A. M. Venezia, D. Andreeva, Gold catalysts supported on CeO_2 and CeO_2-Al_2O_3 for NOx reduction by CO, Appl. Catal. B: Environ. 65 (2006) 101-109.

[31] A. Grosman, C. Ortega, Capillary condensation in porous materials. Hysteresis and interaction mechanism without pore blocking/percolation process, Langmuir 24 (2008) 3977-3986.

[32] S. A. Ansari, M. M. Khan, M. O. Ansari, S. Kalathil, J. Lee, M. H. Cho, Band gap engineering of CeO_2 nanostructure using an electrochemically active biofilm for visible light applications, RSC Adv. 4 (2014) 16782-16791.

List of Figure caption

Fig. 1. X-ray diffraction patterns of Gd_2O_3 (a), Sm_2O_3 (b), CeO_2 (c), sequentially precipitated $Ce_{0.9}Gd_{0.1}O_{1.95}$ (d), $Ce_{0.9}Sm_{0.1}O_{1.95}$ (e) and co-precipitated $Ce_{0.9}Gd_{0.1}O_{1.95}$ (f), $Ce_{0.9}Sm_{0.1}O_{1.95}$ (g).

Fig. 2. Raman spectra of various nanostructures (SP and CP denotes the sequential and co-precipitation).

Fig. 3. HRTEM micrographs of CeO_2 (a-b), Gd_2O_3 (c-d) and Sm_2O_3 (e-f).

Fig. 4. HRTEM micrographs of sequentially precipitated $Ce_{0.9}Gd_{0.1}O_{1.95}$ (a-c) and co-precipitated $Ce_{0.9}Gd_{0.1}O_{1.95}$ (d-f).

Fig. 5. HRTEM micrographs of sequentially precipitated $Ce_{0.9}Sm_{0.1}O_{1.95}$ (a-c) and co-precipitated $Ce_{0.9}Sm_{0.1}O_{1.95}$ (d-f).

Fig. 6. HAADF-STEM micrographs of sequentially precipitated $Ce_{0.9}Gd_{0.1}O_{1.95}$(a), $Ce_{0.9}Sm_{0.1}O_{1.95}$ (b) and the corresponding EDAX images (c-d).

Fig. 7. HAADF-STEM micrographs of co-precipitated $Ce_{0.9}Gd_{0.1}O_{1.95}$ (a), $Ce_{0.9}Sm_{0.1}O_{1.95}$ (b) and the corresponding EDAX images (c-d).

Fig. 8. BET analysis of various nanostructures (SP and CP denotes the sequential and co-precipitation).

Fig. 9. BJH pore size distribution curve for the co-precipitated {(▲) $Ce_{0.9}Gd_{0.1}O_{1.95}$and (x) $Ce_{0.9}Sm_{0.1}O_{1.95}$}, (■) CeO_2 and sequentially precipitated {(▲) $Ce_{0.9}Gd_{0.1}O_{1.95}$and (●) $Ce_{0.9}Sm_{0.1}O_{1.95}$} nanostructures.

Fig. 10. Diffuse reflectance (DR)-UV-Vis spectra of various nanostructures (SP and CP denotes the sequential and co-precipitation).

Fig. 11. Tauc plot of the synthesized nanostructures calculated from the DR UV-Vis spectrum using Kubelka Munk function (SP and CP denotes the sequential and co-precipitation).

List of Table caption

Table.1. BET and BJH characteristics of the sonochemically synthesized nanostructures.

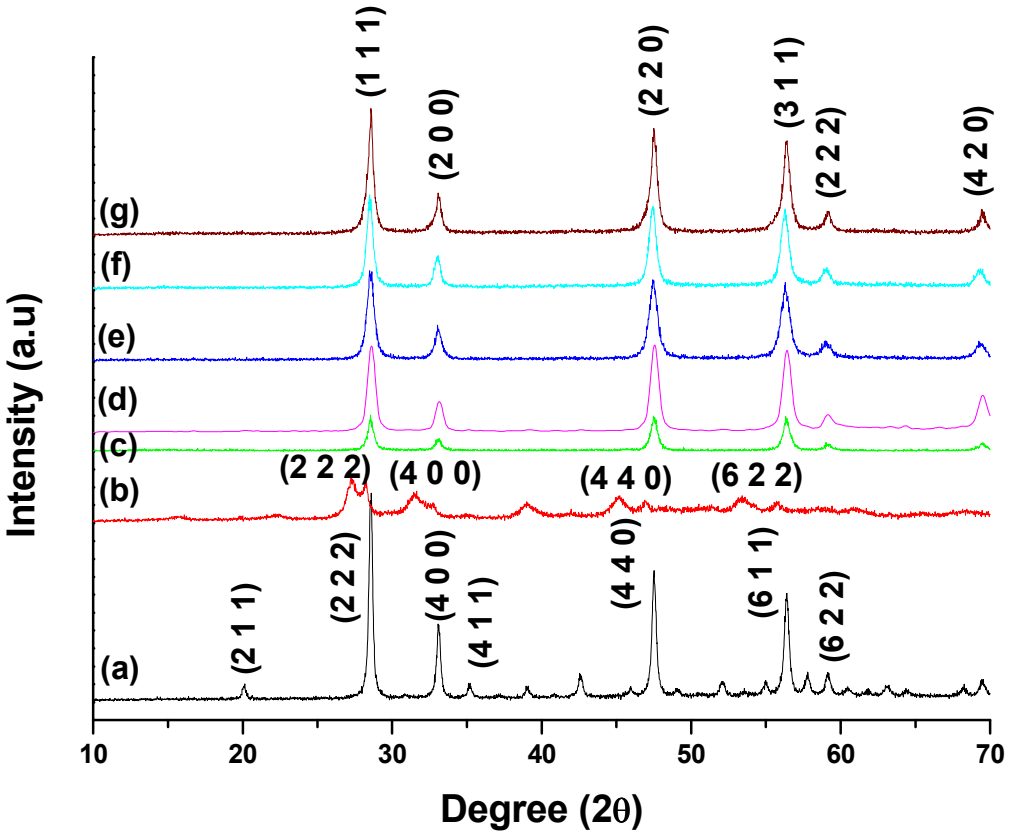

Fig. 1. X-ray diffractions pattern of Gd_2O_3 (a), Sm_2O_3 (b), CeO_2(c), sequentially precipitated $Ce_{0.9}Gd_{0.1}O_{1.95}$ (d), $Ce_{0.9}Sm_{0.1}O_{1.95}$ (e) and co-precipitated $Ce_{0.9}Gd_{0.1}O_{1.95}$ (f), $Ce_{0.9}Sm_{0.1}O_{1.95}$ (g)

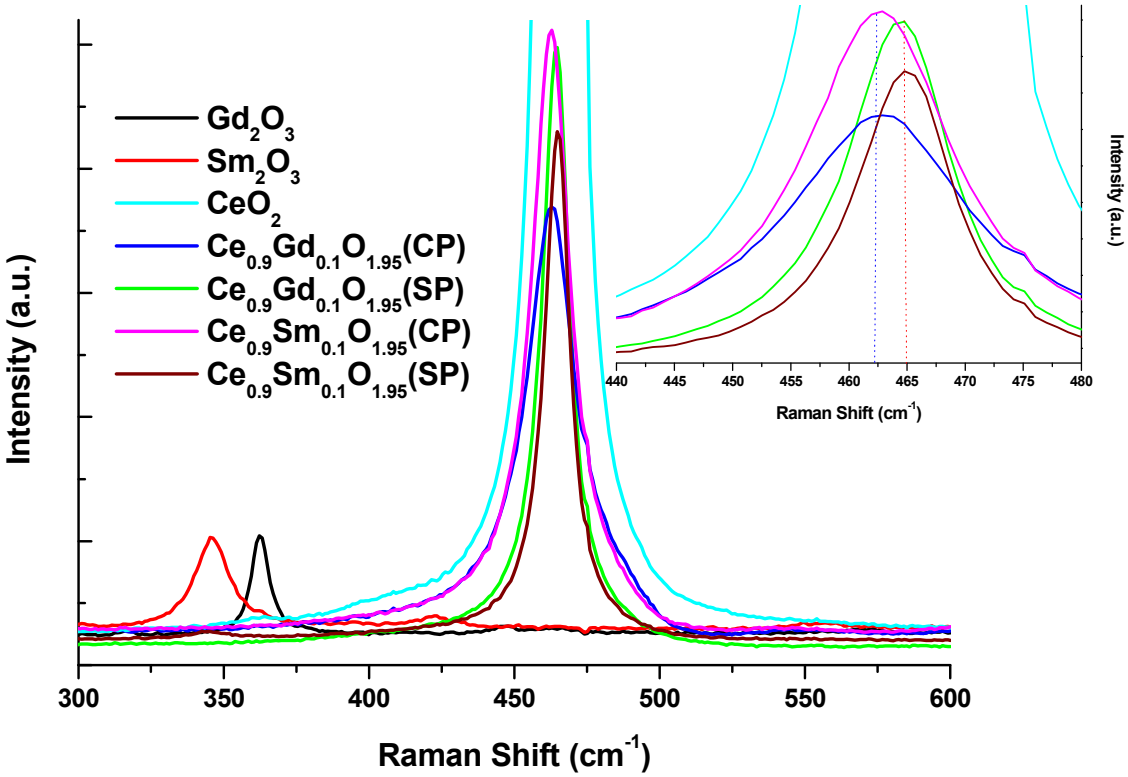

Fig. 2. Raman spectra of various nanostructures (SP and CP denotes the sequential and co-precipitation)

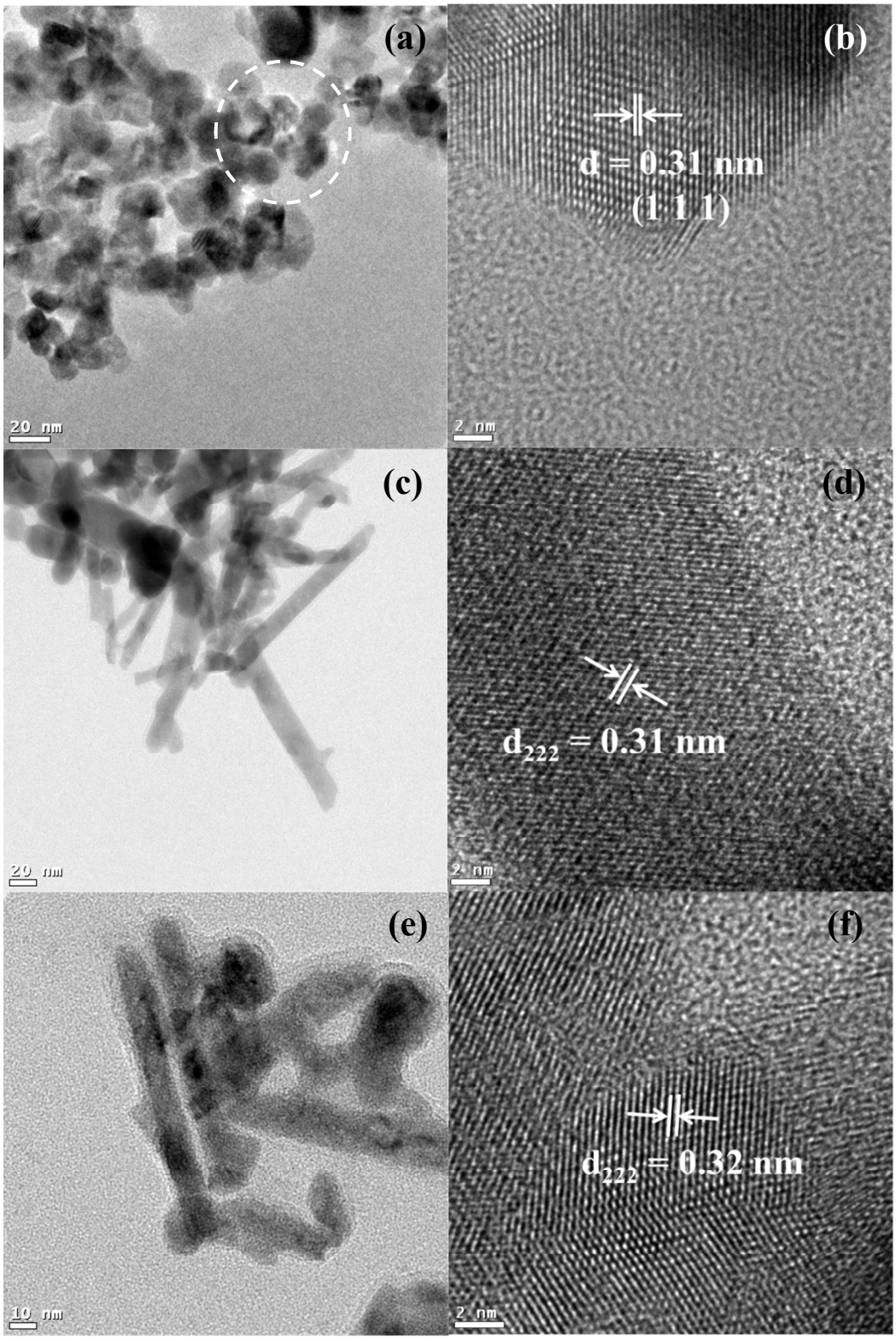

Fig. 3. HRTEM micrographs of CeO_2 (a-b), Gd_2O_3 (c-d) and Sm_2O_3 (e-f).

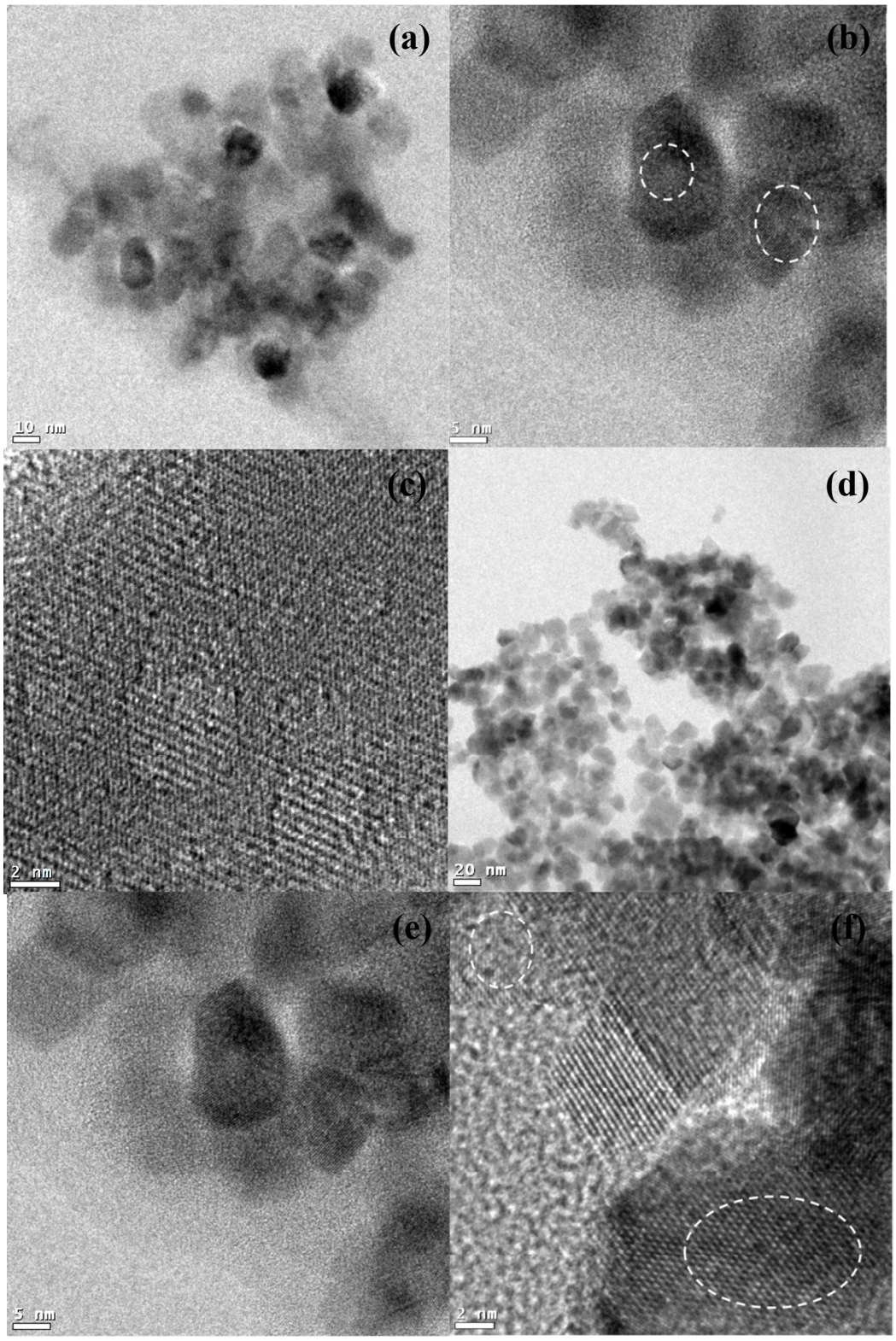

Fig. 4. HRTEM micrographs of sequentially precipitated $Ce_{0.9}Gd_{0.1}O_{1.95}$ (a-c) and co-precipitated $Ce_{0.9}Gd_{0.1}O_{1.95}$ (d-f)

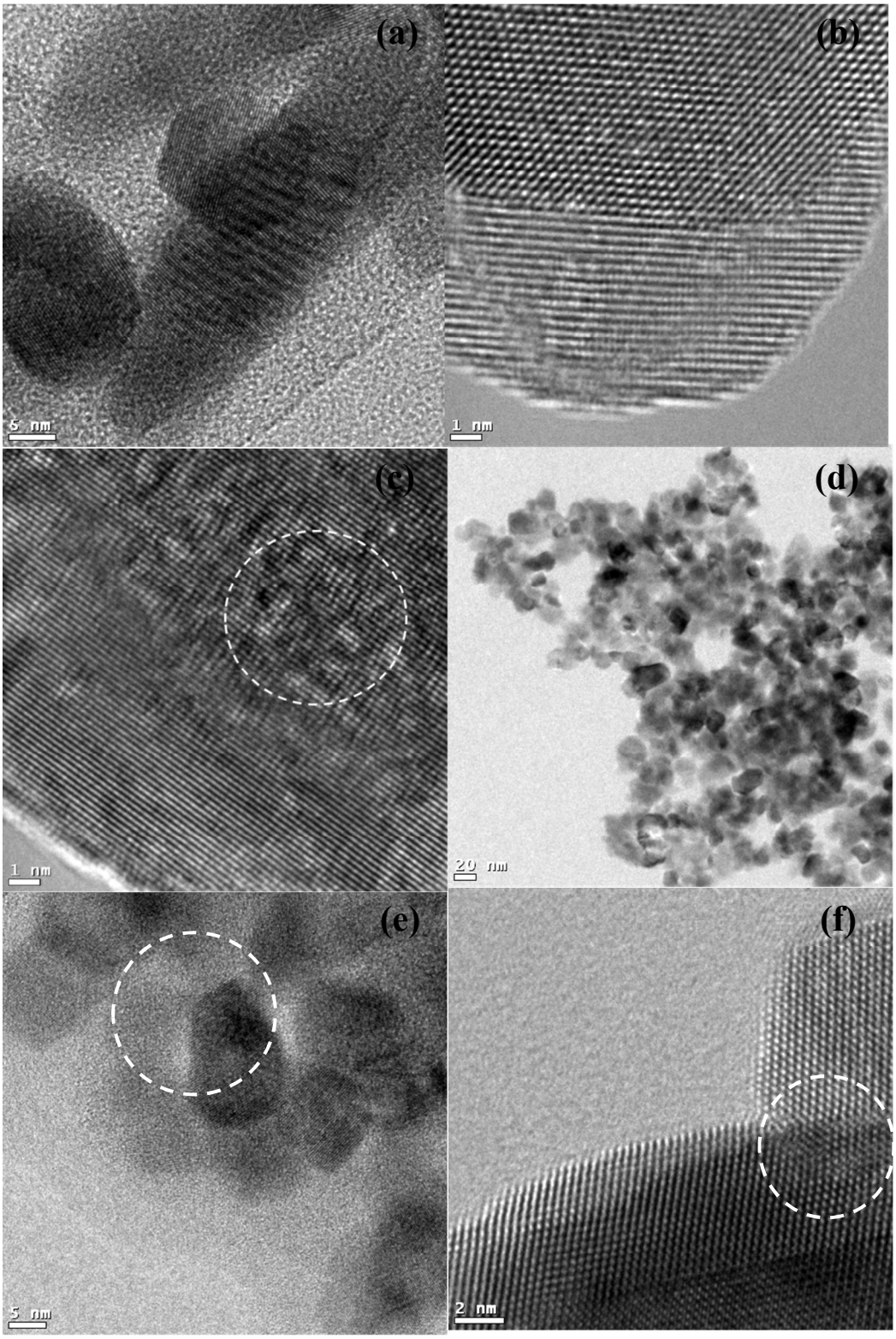

Fig. 5. HRTEM micrographs of sequentially precipitated $Ce_{0.9}Sm_{0.1}O_{1.95}$ (a-c) and co-precipitated $Ce_{0.9}Sm_{0.1}O_{1.95}$ (d-f)

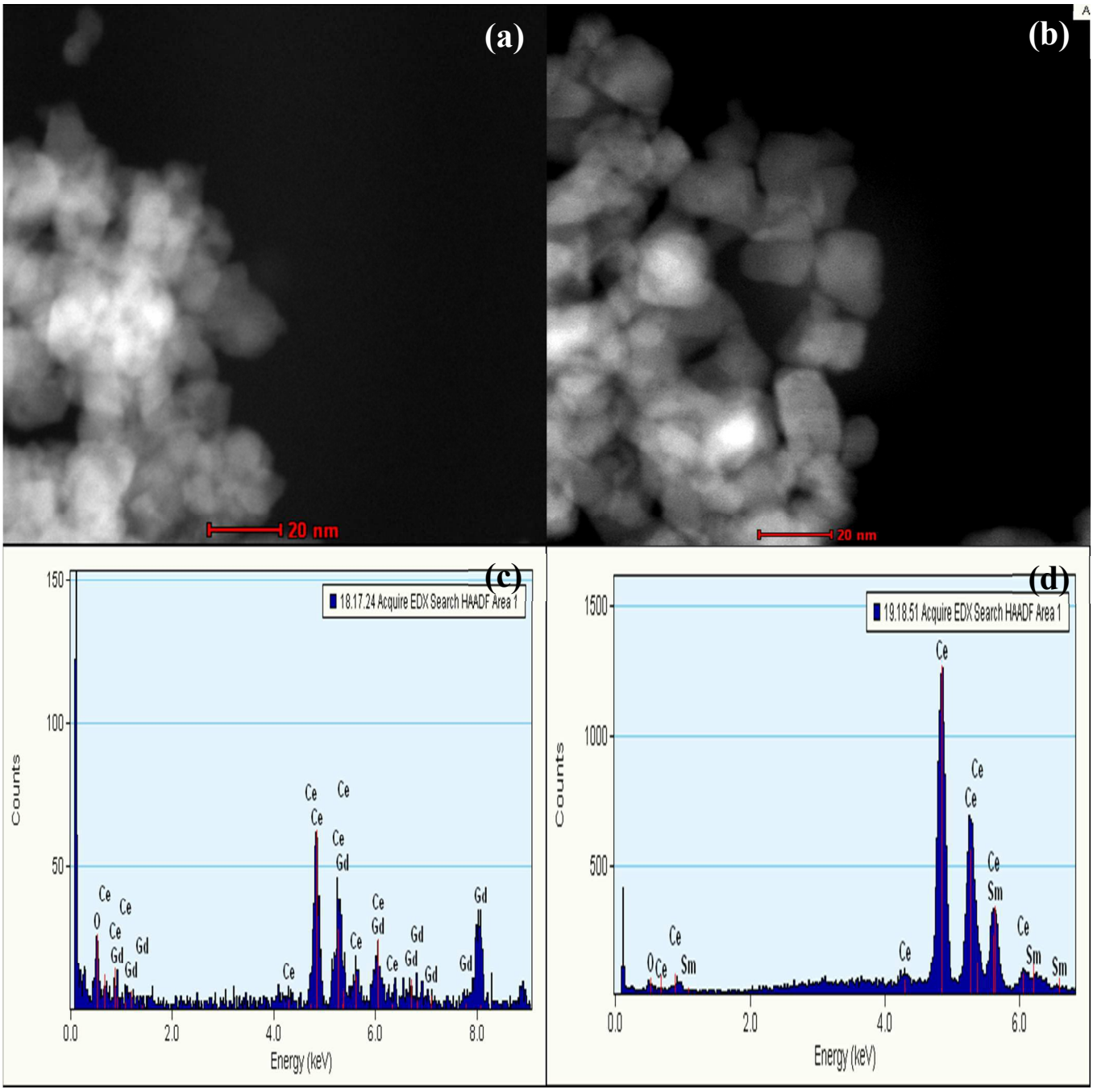

Fig. 6. HAADF-STEM micrographs of sequentially precipitated $Ce_{0.9}Gd_{0.1}O_{1.95}$ (a), $Ce_{0.9}Sm_{0.1}O_{1.95}$ (b) and the corresponding EDAX images (c-d).

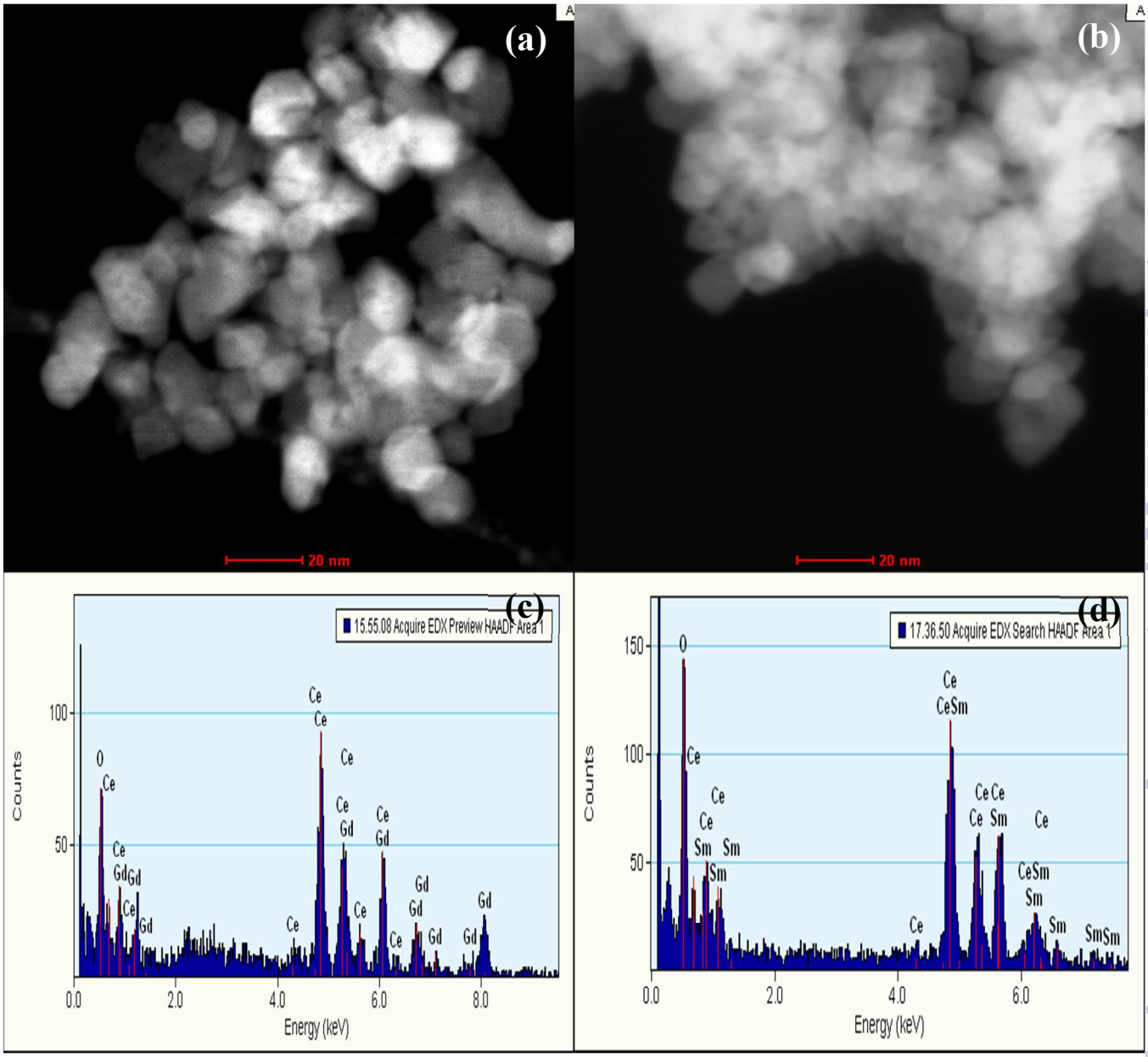

Fig. 7. HAADF-STEM micrographs of co-precipitated $Ce_{0.9}Gd_{0.1}O_{1.95}$ (a), $Ce_{0.9}Sm_{0.1}O_{1.95}$ (b) and the corresponding EDAX images (c-d).

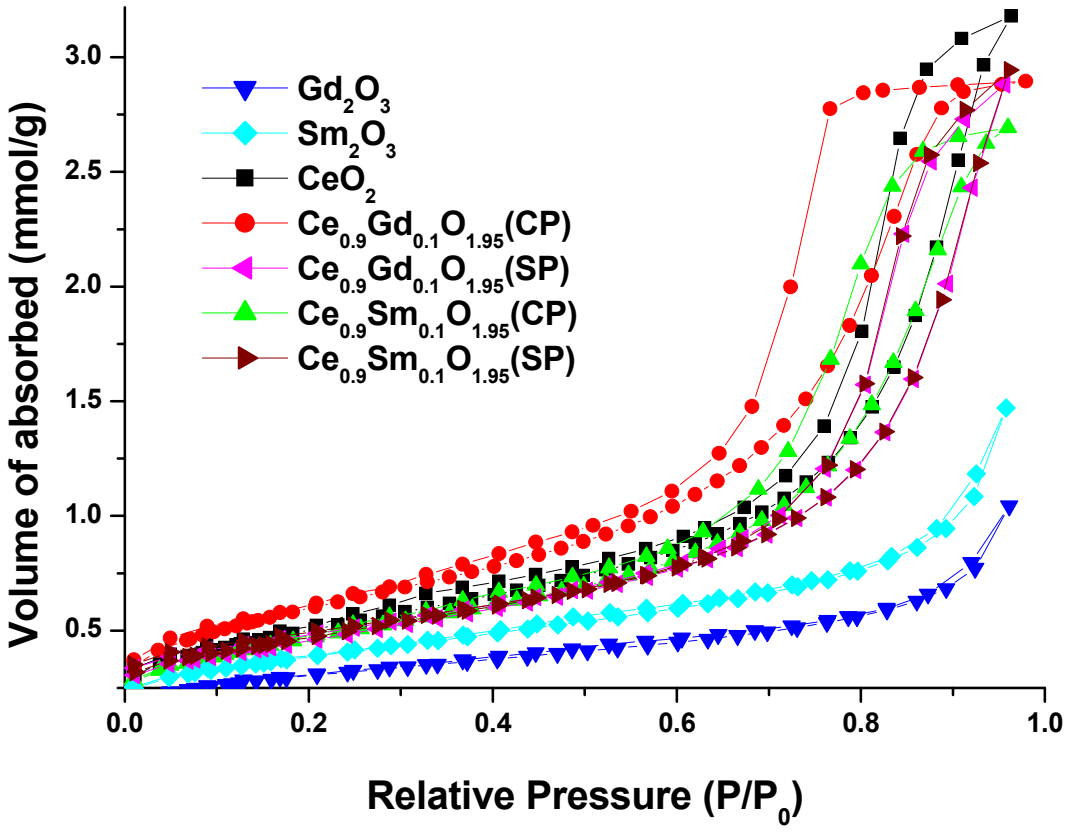

Fig. 8. BET analysis of various nanostructures (SP and CP denotes the sequential and co-precipitation)

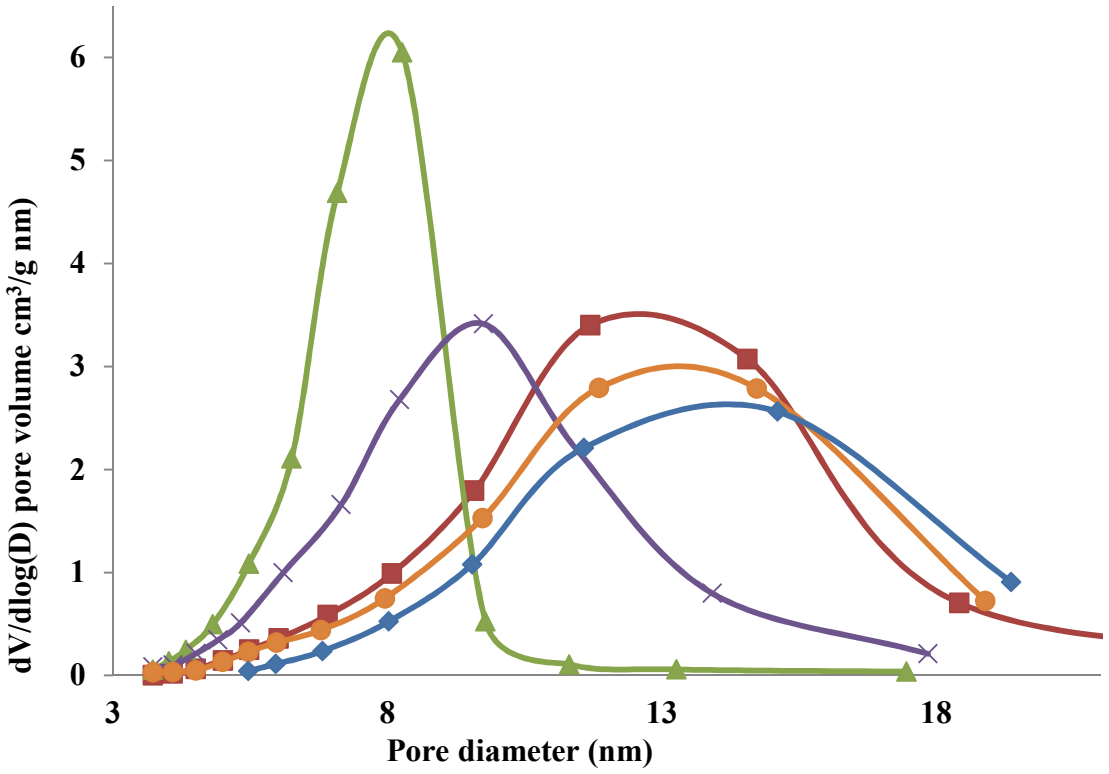

Fig. 9. BJH pore size distribution curve for the co-precipitated {(▲) $Ce_{0.9}Gd_{0.1}O_{1.95}$ and (x) $Ce_{0.9}Sm_{0.1}O_{1.95}$}, (■) CeO_2 and sequentially precipitated {(▲) $Ce_{0.9}Gd_{0.1}O_{1.95}$ and (●) $Ce_{0.9}Sm_{0.1}O_{1.95}$} nanostructures

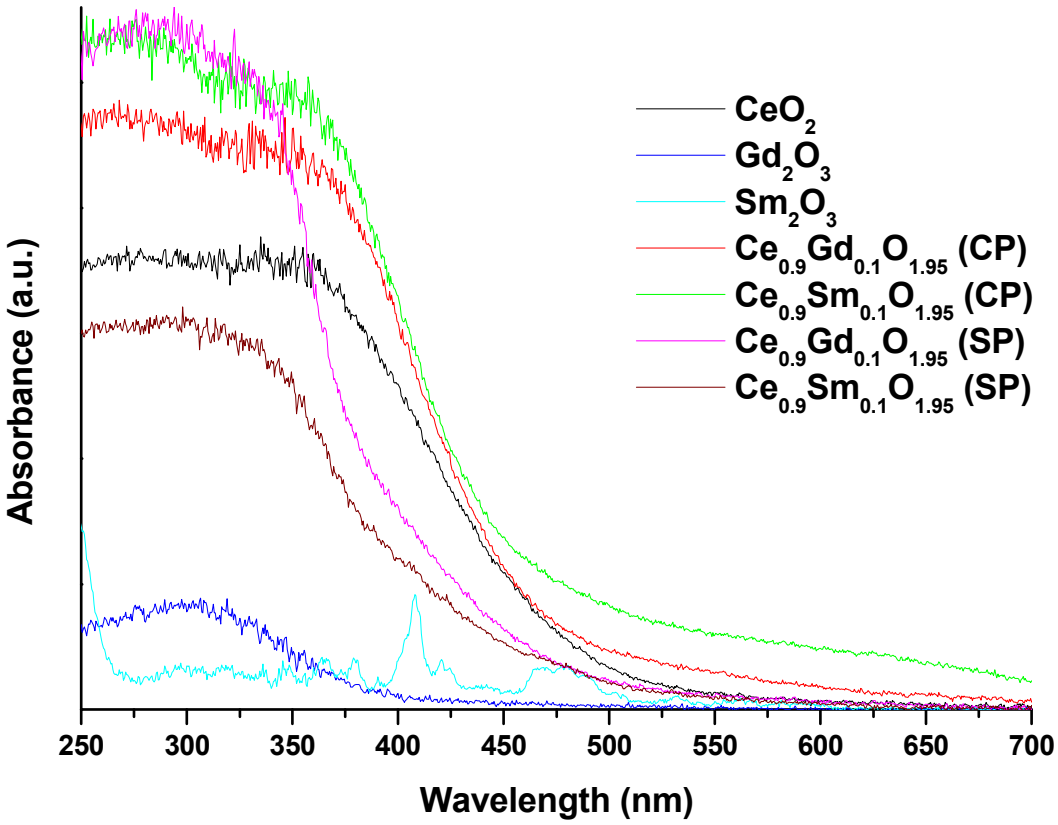

Fig. 10. Diffuse reflectance (DR)-UV-Vis spectra of various nanostructures (SP and CP denotes the sequential and co-precipitation)

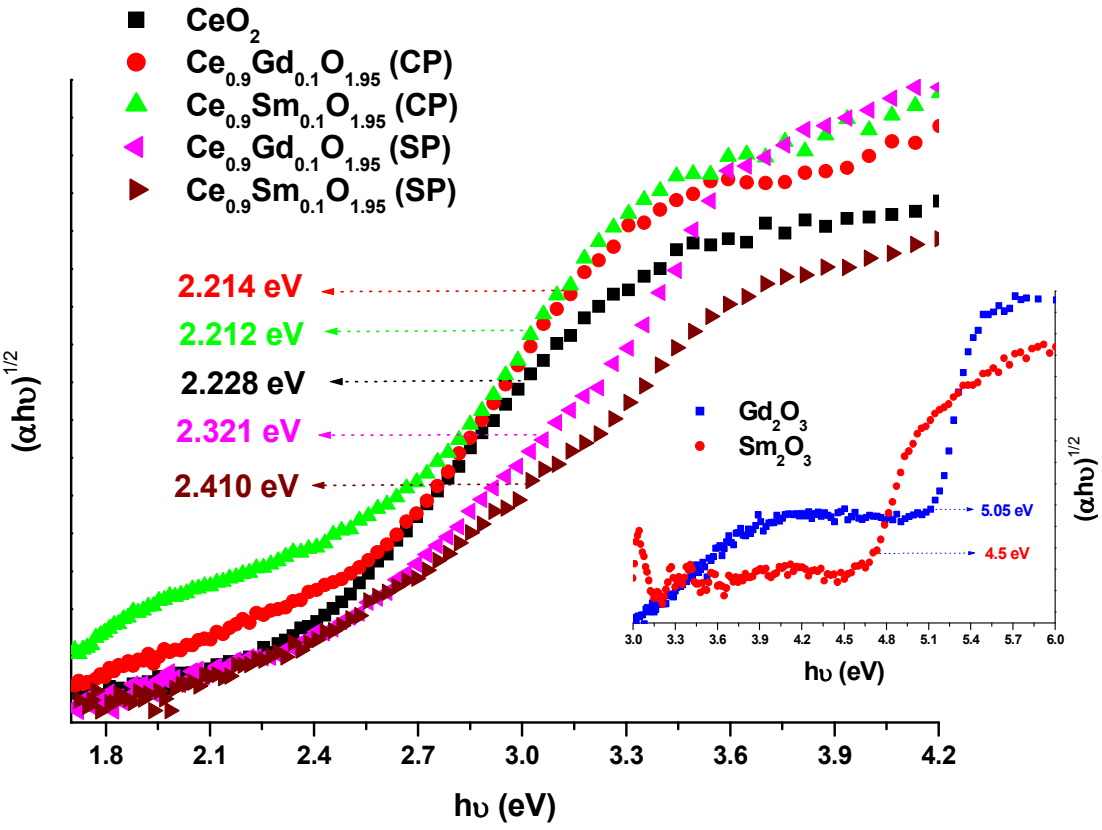

Fig. 11. Tauc plot of the synthesized nanostructures calculated from the DR UV-Vis spectrum using Kubelka Munk function (SP and CP denotes the sequential and co-precipitation)

Table.1. BET and BJH characteristics of the sonochemically synthesized nanostructures

S. No	Nanopowder	BET Surface Area (m^2/g)	Total Pore Volume (cm^3/g)	Micropore Volume (cm^3/g)	Mesopore Volume (cm^3/g)	Pore diameter (nm)
1.	CeO_2	41	0,11	0,02	0,09	11.7
2.	$Ce_{0.9}Gd_{0.1}O_{1.95}$ (CP)[5]	48	0,10	0,02	0,08	8.3
3.	$Ce_{0.9}Sm_{0.1}O_{1.95}$ (CP)[5]	38	0,09	0,02	0,08	9.7
4.	Gd_2O_3	23	0,04	0,01	0,03	7.1
5.	Sm_2O_3	30	0,05	0,01	0,04	7.1
6.	$Ce_{0.9}Gd_{0.1}O_{1.95}$ (SP)[6]	36	0,10	0,02	0,08	11.9
7.	$Ce_{0.9}Sm_{0.1}O_{1.95}$ (SP)[6]	37	0,10	0,02	0,08	11.8

[5] Co-precipitation

[6]Sequential precipitation